

# Chapter 1

## Electron Tomography: A Primer

Andrew Leis

**Abstract** This chapter is an introduction to the theory and practise of electron tomography. It identifies the areas in need of most attention to maximise the efficiency of descriptive studies of morphology, and in the case of structural biology, to enable the transition from a reductionist approach to in-depth systems biology. The chapter concludes with a step-by-step guide to acquiring tomograms.

### 1.1 An Introduction to Electron Tomography

Electron tomography provides the unique possibility to view three-dimensional (3D), nanometre-scale detail within the cellular context (for detailed reviews, see [1–3]). It is one of a small group of bioimaging technologies that utilise electrons or photons to deliver 3D information about structural complexity spanning macromolecules, viruses, cells and tissues. These techniques include confocal microscopy, some forms of super-resolution microscopy, and soft X-ray tomography, albeit with differing means of generating contrast, and overlapping resolution. With proper attention to structural preservation, these techniques are capable of capturing and deciphering cellular events such as the workings of protein machines in healthy cells [4] and in disease, a special case being the morphogenesis of infectious agents [5–8]. The common feature of these techniques is the ability to image hydrated (or frozen-hydrated) specimens. Confocal and super-resolution microscopy techniques visualise fluorescent ‘spots’ rather than actual densities but they also provide unambiguous identification and possibly some temporal resolution. Furthermore, the spatial information can be decisive, as is the case for fluorescence (‘Förster’) resonance energy transfer (FRET) analysis of protein-protein interactions [9]. Cryo- electron tomography captures snapshots of true densities within the cellular landscape but given the prospects for macromolecular crowding, especially in prokaryotes [10, 11]

---

A. Leis (✉)  
CSIRO Australian Animal Health Laboratory,  
Private Bag 24, Geelong, VIC 3222, Australia  
e-mail: leisandrew@gmail.com

and the similarities of many complexes at the best, attainable resolution, it can be more difficult to assign structure or determine interactions without explicit, *a priori* information. Therefore, this group of techniques should be considered together as a complementary and powerful means of determining structure-function relationships in cells [12]. Correlative light and electron microscopy (CLEM, [13–17]) seeks to apply such technologies in combination for the elucidation of structure-function relationships.

From an instrumentation perspective, electron tomography belongs to the group of electron microscope -based technologies capable of generating 3D structures, collectively referred to as ‘3D electron microscopy’ (3DEM, [18]). 3DEM comprises four, independent strategies (Fig. 1.1). Three of these utilise a transmission electron microscope (TEM) as a projection device, while a third uses a scanning electron microscope (SEM). The first of the TEM strategies—electron tomography—constitutes the main theme of this book. The second TEM technique employs a scanning transmission electron microscope (STEM, Wolf, Chap. 2). This technique has the advantage of being able to analyse thicker specimens and with enhanced contrast

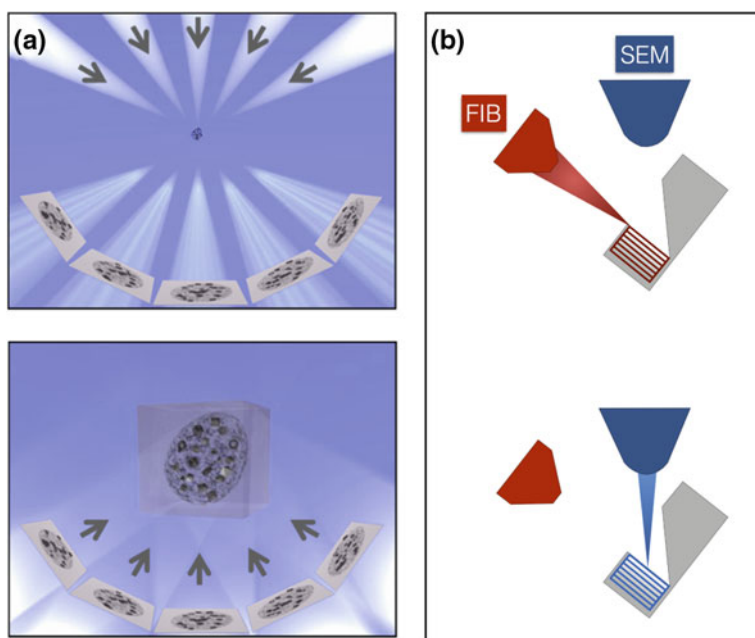


**Fig. 1.1** Imaging geometries for electron tomography. **a** TEM and STEM tomography. 2D projections acquired from a 3D object (upper panel) are back-projected to provide the solution to the structure (reproduced from [1], with permission from Nature Publishing Group); **b** serial-block-face SEM tomography. Fresh layers of the specimen are removed (sputtered) sequentially using a focussed gallium ion beam (FIB). As each layer is removed, the freshly revealed block surface is imaged by a scanning electron microscope (SEM) to build up a 3D volume

compared to bright-field TEM [19, 20], noting that phase plates now offer a solution for the latter. A third TEM technique—single-particle analysis (SPA)—should be considered separately as a powerful means of determining the structures of identical or nearly identical copies of macromolecules or symmetrical (principally, icosahedral) viruses. SPA will be discussed briefly to introduce certain concepts, and for the sake of completeness. The SEM tomography technique, serial block-face imaging, utilises a scanning electron microscope in conjunction with a sectioning device, either a diamond knife [21] or an ion beam [22–26], to build up a three-dimensional volume, layer by layer, analogous to the operating principle of a confocal microscope. At present, this technique is practised on plastic-embedded specimens. It is covered in detail in Chap. 5. To complete this short overview of tomography strategies, it is worth mentioning the technique known as ‘array tomography’. Although best known from fluorescence microscopy, it is equally applicable to the serial-block-face technique or indeed, in combination (Chap. 6). It allows large-scale surveys of classical ultrastructure afforded by serial block-face imaging but in combination with the mapping of fluorescent epitopes. Like serial block-face imaging, however, it is not suited to studies of molecular structural biology.

Finally, we can define a category of biophysical techniques that provide superior resolution to electron tomography but with the caveat that the structures are generated from isolated and purified entities that are thus removed from the cellular context. The resulting structures can be used for visual proteomics interrogations of cellular interaction networks. These techniques are the standard techniques of structural biology, and include X-ray crystallography as well as single-particle analysis (cryo-) electron microscopy. As mentioned above, SPA is a reductionist approach to solving structure that takes advantage of statistical sampling *ex vivo*. The term ‘single-particle’ is a misnomer because the technique takes into account as many particles as can be sampled efficiently, typically tens of thousands, rather than a unique occurrence of a molecule within its native context. SPA is related to cryo-electron tomography in terms of common sample preparation and bright-field, low-dose imaging conditions. It may begin with air-dried and stained preparations because these structures serve as useful starting models for computational refinement of frozen-hydrated data. Unlike X-ray crystallography, SPA does not have a requirement for crystals, and it can cope with large, multi-unit complexes as well as some heterogeneity. For comprehensive reviews of SPA in structural biology and virology, the reader is referred to detailed reviews [27–33]. Modern structural biology increasingly aims to harness the synergies of these techniques when used in combination (‘hybrid techniques’, [34]). In particular, the high-resolution structures can be used to populate tomograms of cells via the process of pattern recognition in real space (see ‘Template Matching’). Thus, it is important to consider tomograms generated by electron tomography as complete maps of a cell’s proteome, where (dose-) limited resolution can be circumvented to produce a ‘pseudo-atomic atlas’ of the macromolecular machinery that underlies cellular function [1].

The definition of electron tomography used in this book includes TEM/STEM tomography as well as the newer SEM strategies. It therefore expands upon the

definition provided in the most recent textbook on electron tomography [18], which suggests that it should loosely incorporate strategies where the specimen is tilted. The revised definition reflects the recent success of approaches for building up 3D volumes by SEM, which was previously regarded almost exclusively as a ‘surface’ technique. This chapter will introduce the principles of TEM- and SEM-based electron tomography, recent technological developments, and selected contributions to cell and structural biology. It cannot possibly do justice to the published applications of electron tomography. For recent, general reviews, the reader is referred to references [3, 35]. Other recent reviews cover application of electron tomography to viruses [30, 36] and prokaryotes [37], while newer publications enabled by low-temperature nanofabrication showcase novel insights and possibilities for the biology of ‘higher’ organisms [38–41].

## 1.2 Principles of Electron Tomography

The TEM strategy for electron tomography is analogous to medical X-ray imaging (computed tomography—‘CT’ or ‘CAT’ scans) in that it uses projections of a specimen recorded from different viewing angles and back-projects them into Fourier Space (syn. frequency domain) to calculate a real-space (syn. position space) reconstruction of the ‘specimen’ (Fig. 1.2). The main difference to computed tomography in terms of image acquisition is the tilting of the specimen in electron tomography compared to tilting of the imaging gantry during computed tomography, although a concept for a tilting electron microscope has been published [42]. Note also that ‘soft’ X-ray tomography of cells utilises a fixed X-ray source or synchrotron beamline and either a rotating or tilting sample holder. A TEM goniometer and sample holder are used for the latter. TEM tomography is used routinely for specimens that have undergone a substitution process to replace the sample’s water with a plastic resin, which in turn can be sectioned and introduced into the microscope using a standard sample holder. This technique is useful for studies of ultrastructure, such as the arrangements of organelles [43] or studies of *e.g.* membranes during virus morphogenesis [44, 45]. A variation of this protocol with additional contrast agent is used for serial-block-face SEM tomography [46] (see Chap. 5 and below). Cryo- electron tomography (or electron cryotomography, Chap. 3) is the method of choice for appropriately thin, frozen-hydrated specimens, where structural accuracy is paramount, *i.e.* the density map reflects the true nature of the feature rather than added contrast agent, the accumulation of which depends on its relative affinity for the different regions of a molecule.

So-called ‘single-particle analysis’ 3D electron microscopy uses projections of many copies of identical or nearly identical, frozen-hydrated macromolecules or viruses to build up a 3D reconstruction. This powerful, biochemical reductionist approach combines computational averaging of many copies of identical or nearly identical, randomly orientated molecules with statistical suppression of noise to generate a composite structure of the molecule at a resolution typically better than

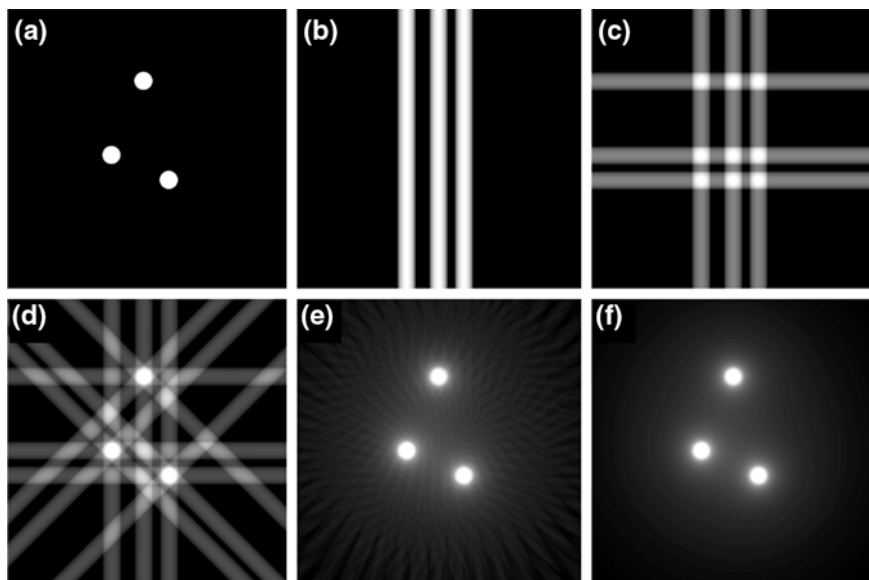


**Fig. 1.2** Application of the Radon Transform to mock, 2D data (adapted from Linaroudis [47]). **a** Original ‘features’; **b** one projection; **c** 2 projections; **d** 4 projections; **e** 45 projections; **f** 180 projections. In each case, the projections are equidistant and span the full angular range

10 Å (reviewed in [31, 33, 48]). The sample is usually not tilted; exceptions are the random conical tilt and related orthogonal tilt methods [49]. Instead, the typically reasonable assumption is made that the macromolecules or viruses lie in random orientations with respect to the beam. These different views of the ‘same’ structure contribute more or less equally to the structure solution, and deviations from similarity become apparent in the ‘class averages’ representing the different orientations. Apart from its similar requirements for a TEM and image processing, single-particle analysis bears little relationship to the subject of this book, electron tomography, except that the structures it generates can be used to populate tomograms of cells in the strategy known as ‘visual proteomics’ [1, 38, 50–53]. As such, it belongs to a separate category of nominally ‘high-resolution’ techniques that includes X-ray crystallography but also NMR spectroscopy. Another reason for mentioning it here is that similar computational approaches can be applied to symmetrical and/or repetitive structures in tomograms to enhance local resolution. This is known as subtomogram averaging [54], and forms the subject of Chap. 9.

The structure of the Herpes simplex virus (Fig. 1.3) provides an elegant demonstration of this approach because each mature virus contains both pleomorphic and symmetrical components [55]. The resolution for the symmetrical components can be enhanced post-acquisition. Thus, even though electron tomography produces a comparatively modest resolution compared to single-particle analysis of wholly symmetrical viruses [56], it is unique in its ability

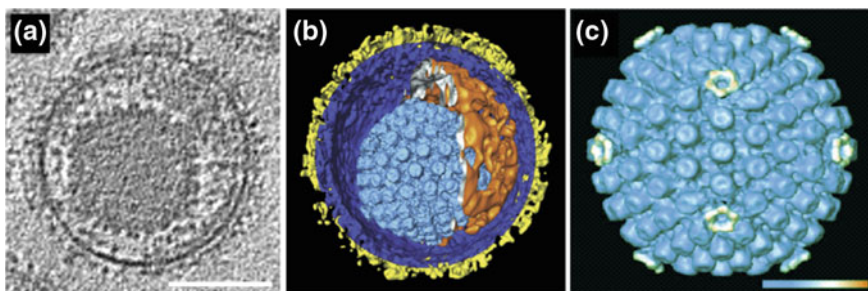


**Fig. 1.3** Electron tomography samples pleomorphic and symmetrical structures. The three-dimensional structure of individual herpesviruses at modest resolution was sufficient to visualise individual glycoprotein spikes (yellow) on the virus surface. Computational extraction of a modest number of nucleocapsids ( $n = 11$ ) followed by averaging and applying icosahedral symmetry resulted in a substantial improvement in local resolution [55]. Scale bar = 100 nm. Reproduced with permission from the American Association for the Advancement of Science

to generate structures for pleomorphic specimens at a resolution of better than 10 nm. Furthermore, tomograms of cells can be archived and refined locally when improved structures become available. In the context of cell biology and virology, this is extremely important: all cells are pleomorphic, and they are subject to stochastic variability. They may contain symmetrical or repetitive structures, *e.g.* icosahedral viruses but tomography is needed to visualise the cellular landscape. On the other hand, the use of single-particle averaging for determining the structure of wholly symmetrical viruses is well established and represents a mature technology [57].

### 1.3 Sample Preparation for Electron Tomography

The ability of electron tomography to generate authentic structures at a resolution of better than 10 nm emphasises the requirement for suitable, resolution-preserving sample preparation procedures. All forms of sample preparation require a fixation (immobilisation) step to stabilise the structures and maintain their spatial relationships when introduced into the vacuum environment of the electron microscope. The classical approach is chemical fixation using aldehyde-based cross-linkers, which are easily criticised as artefacts. Physical immobilisation by rapid freezing can be used instead, and it is used exclusively for cryo- electron tomography, as well as for single-particle analysis. In brief, vitrification means that with sufficiently fast cooling rates, water is transformed into an amorphous solid that is thought to resemble liquid water, and which is (meta) stable during controlled image acquisition. This is referred to as the ‘frozen-hydrated’ state.

Before discussing the different methods for acquiring, aligning, reconstructing and segmenting tomograms (see following sections), it is first necessary to mention

the characteristics of the specimens that determine the imaging conditions and image-processing strategies. For example, beam-sensitive, frozen-hydrated specimens require a dedicated, low-dose acquisition scheme, and the resultant noisy reconstructions benefit from denoising to aid in surface rendering ('segmentation', see later). Stained plastic sections of membrane-rich cells, on the other hand, are more amenable to automated segmentation routines; these are suitable for characterising ultrastructure rather than studying molecular arrangements and interactions.

### ***1.3.1 Scenario 1: Plastic sections***

The classical TEM protocol developed for biological samples comprises aldehyde fixation, dehydration in a graded alcohol series, infiltration with resin, heat-induced polymerisation and sectioning using an ultramicrotome. This procedure was the mainstay of biological electron microscopy in the second half of the twentieth century [58], and with mostly subtle variations, it continues to be the most widely used strategy for studies of cell ultrastructure. Refined versions of this protocol bypass chemical fixation in favour of rapid freezing and progressive solvent substitution at low temperature, culminating in a UV-polymerised resin block that can also be sectioned by ultramicrotomy. This improvement avoids the artefacts of chemical fixation, although it is difficult to study alterations that occur after freezing. As for any vitrification process, with or without added cryoprotectant, it depends critically on specimen thickness. Nevertheless, the freeze-substitution process has been studied systematically from a process perspective, and it was shown that the processing time can be reduced from days to as little as 3 h [59]. Structural preservation after freeze-substitution is clearly superior to structure visualised after the use of chemical fixatives. In either case, sections need to be cut as thin as possible without eliminating the feature of interest. In practical terms, this is dictated by the accelerating voltage of the microscope. Sections of nominal thickness 80–90 nm are suitable for electron tomography using a 120 kV TEM, whilst thicknesses up to 300 nm represent the maximum thickness for use in 300 kV instruments whilst still avoiding the possibility of multiple scattering events [52] that degrade resolution.

Although freeze substitution is superior to classical fixation and embedding, it is highly informative to revisit the use of powerful (1 MV) transmission electron microscopes as projection devices but without the benefits of adequate structural preservation. This led to the flawed 'microtrabecular lattice' concept of cell structure [60]. Here, removal of solvent and/or fixation with glutaraldehyde caused the soluble components of the cytosol to be deposited on elements of the cytoskeleton, portraying mammalian cells erroneously [61] as an irregular network of cross-linked 'microtrabeculae' (Fig. 1.4). Porter interpreted these observations as the fundamental organisation of the cytoplasm, the physical basis for cytoplasmic motility, and the determinants of cell shape [61]. In the absence of tomography, he made use of stereo pairs to demonstrate his results.



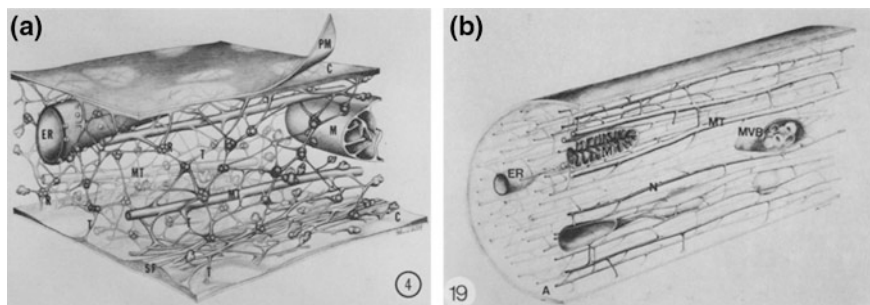


**Fig. 1.4** Models of Porter's microtrabecular lattice [60] and axonal lattice [62]. The decorated cytoskeleton is largely the result of soluble components of the cytosol having 'nowhere to go', and agglomerating onto the cytoskeleton. Crosslinks are also difficult to reconcile. Reproduced with permission of The Rockefeller University Press

Porter's rather exhaustive efforts to corroborate his findings preceded cryo-EM, and they did not survive scrutiny when it was shown that similar features could be induced in homogeneous solutions of serum albumin [63]. The methods that led to the erroneous microtrabecular lattice concept have been superseded by cryofixation followed by freeze-substitution, or by cryo-EM. At present, only cryo-EM of a sufficiently thin, vitreous specimen can guarantee a faithful reproduction of the cell interior. New technical developments in cryo-EM are beginning to allow the study of eukaryotic cells [39, 40, 64, 65].

### 1.3.2 Scenario 2: Frozen-hydrated specimens

Electron tomography of frozen-hydrated specimens is detailed in Chap. 2. Most commonly, the specimens (isolated macromolecules, viruses, organelles; intact cells) are vitrified by plunging into liquefied ethane. If sufficiently thin—as dictated by the accelerating voltage—tomograms can be recorded directly. Thicker, frozen-hydrated cells can be thinned on the sample support grid using a cryogenically-cooled focussed ion beam setup prior to transfer to the TEM (see [66] for details). Alternatively, a cellular sample can be vitrified by high-pressure freezing and then vitreously sectioned using *e.g.* a cryo-ultramicrotome. For all manipulations that follow the vitrification step, it is essential to maintain the specimen at a temperature colder than the devitrification temperature ( $-137^{\circ}\text{C}/136\text{ K}$ ) to avoid a phase transition from an amorphous state to cubic crystalline ice. Focussed ion beam (FIB) sample fabrication at cryogenic temperatures is an emerging technology that is still practised by a handful of specialist cryo-tomography laboratories but its benefits have been realised recently [67–69], and they are highly convincing. The major breakthrough is that it enables studies of plant and animal cells by cryo-electron tomography where previously, the technique was restricted to isolated macromolecules, viruses and small cells such as bacteria that could be plunge frozen from suspensions and visualised directly [66]. Where available,



cryo-FIB followed by TEM tomography essentially supersedes cryo- electron microscopy/tomography of vitreous sections (CEMOVIS/CETOVIS) because it does not suffer from the unavoidable artefacts that plague knife-cut sections. These include significant compression (>30%), and further deformations that occur during cutting or attachment to a support grid. Nevertheless, tomography of vitreous sections led to key breakthroughs including the first demonstration of ATP synthases in mammalian cells [64], and the discovery of the mycobacterial outer membrane [70, 71].

## 1.4 Radiation Damage

An electron beam represents a form of ionising radiation, collimated into a small area such that all specimens, whether frozen or plastic-embedded, are prone to significant and irreversible damage. In TEM tomography, the need to acquire all of the projections from the identical region of interest places an ultimate limit on the amount of information that can be acquired. It is therefore critical to know how to measure and control the electron dose, and to keep this dose at subcritical levels. In frozen-hydrated specimens, radiation (colloq., ‘beam’) damage can be seen in the form of gas bubbles that are generated as a result of radiolysis. Perhaps more critically, this is preceded by more subtle damage that can erase fine detail. The consequence of an upper limit to the cumulative electron dose is that it must be estimated before exposure of the specimen. Too little dose may lead to difficulty in acquisition (failed position tracking, for example) but more importantly, it results in a poor yield of information. The cumulative dose during tilt-series acquisition should not exceed  $100 \text{ e}^-/\text{\AA}^2$  [3].

For plastic sections, deformations in the form of shrinkage and mass loss are profound [72]. It is common practice to pre-irradiate the specimen, which allows it to undergo a rapid shrinkage phase before acquisition of the tilt series. Here, successful alignment of tomograms is dependent on comparatively minor changes between subsequent projections. This practise is addressed systematically in Chap. 4. In the author’s experience, a tomographic reconstruction of an Epon section with nominal (microtome) section thickness of 150 nm will approximate 110 nm, even when using low-dose acquisition techniques and cooling the specimen in a cryo- sample holder. The final thickness also appears to be quite variable. Quantitation from plastic sections is not possible without bold assumptions concerning distortions. Furthermore, these distortions are not isotropic. Even for pre-irradiated plastic sections, it is advisable to use low-dose acquisition techniques as described below. This helps to facilitate subsequent alignment.

## 1.5 Acquisition of Projections

We have already noted that tomograms comprise multiple views of the same object. We will first discuss the considerations for acquisition of cryo tomograms. Gordon *et al.* [73] summarise the electron tomography problem as the necessity to “reconstruct

a picture from a finite subset of its projections taken at distinct angles.” Completeness of information, however, depends on sampling statistics. For cryo- electron tomography, this is an apparent paradox. The requirement for as many projections as possible while covering the full angular range conflicts with the need to keep the electron dose at subcritical levels to avoid erasing details. This means that a finite electron dose is typically fractionated over the available tilt range. The “dose fractionation theorem” [74, 75] states that the dose tolerated by the specimen can be divided by the number of contributing projections to provide the maximum permissible dose for any one projection image of the tilt series. A negligible proportion of the dose is expended on secondary tasks such as searching, tracking, and focussing, and ideally, tracking and focussing are performed at adjacent positions along the tilt-axis (Fig. 1.5) so that all of the available dose is used for acquiring structural information. Projection images obtained with a low-dose collection strategy have poor signal-to-noise (SNR) characteristics; however, contrast is restored by tomographic reconstruction and subsequent visualisation of each “virtual” slice. Energy filters operating in “zero-loss”

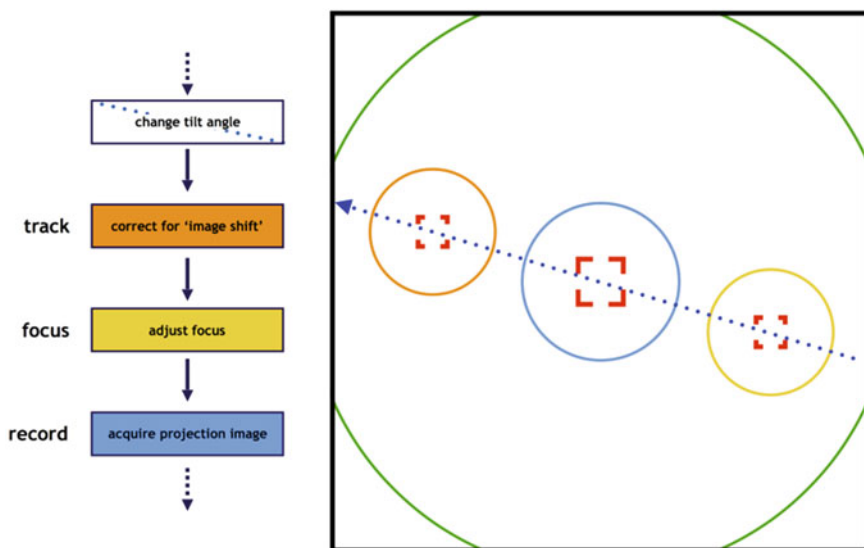


**Fig. 1.5** Schematic of simplified acquisition scheme for low-dose electron tomography. After searching for the region of interest (outer circle indicating spread beam and low flux), the beam position and other parameters for the exposure are copied to focus and tracking states, which are positioned along the tilt axis using the image shift function. The beam is then re-directed to the detector for these ‘off-axis’ states. This restricts all secondary tasks to areas adjacent to the target region, meaning that exposure of the target is solely for the purposes of collecting data. The beam blank function is used to ensure that exposure is limited to the times specified (while reading out the data, for example). The areas captured by the detector are shown by photo corners, and the tilt axis is indicated by a blue dotted line. To expedite the process, modifications such as comparatively higher dose and partial detector readout are commonly made to the tracking and focus states. Also, it is possible to identify multiple targets and automate serial tomogram collection

mode remove contributions from inelastically scattered electrons [76] that cause image blur. The combination of moderate accelerating voltage (300 kV) and an energy filter therefore compensate for the poor SNR characteristics inherent in frozen specimens. They also facilitate tomography on slightly thicker specimens but with a concomitant trade-off in resolution. Note that, for unstained (cryo) specimens, SNR is discussed in preference to contrast, the latter of which can be enhanced artificially. Contrast enhancement does not suppress noise.

In cryo- electron tomography, the radiation sensitivity of the frozen-hydrated specimen means that tomograms comprise only about half as many projections as for plastic sections, collected at increments of 1.5 or 2 degrees. Further complications arise from the increase in apparent thickness of the slab-shaped sample during tilting and ultimately, the limited range of the tilt holder/sample grid combination. This gives rise to the so-called “missing (information) wedge”, which describes the unsampled region in Fourier space. The information deficit results in a real-space artefact whereby features parallel to the electron beam appear to be smeared, while features orthogonal to the beam are unresolved. A  $\pm 70^\circ$  tilt range provides 78% of the available information but with an anisotropic, *i.e.* biased, representation of information. A dual-axis acquisition scheme [77, 78] addresses the fundamental geometric bias. In this acquisition scheme, a complementary series of projections is acquired from the orthogonal axis and merged with the initial tilt series. If the second tilt series covers a similar angular range, dual-axis tomography improves sampling to 93% of the corresponding Fourier space [79], and the resolution is more isotropic. Long, filamentous structures such as microtubules are resolved equally well, regardless of whether they are parallel to the tilt axis or perpendicular.

Much of the preceding discussion is applicable to plastic sections, although the beam damage experienced is more subtle in the sense that it is deceptively gradual and to the novice, might go unnoticed. It is not less important. For plastic-embedded sections, a tomographic tilt-series may comprise more than 150 separate projections collected at  $1^\circ$  increments. If we assume that the sample thickness remains constant, 150 similar exposures corresponds to 150 times the electron dose for a single projection. In practise, it is much higher due to the increased beam cross-section at progressively higher tilt, where thickness is related to the cosine of the tilt angle. Thus, although the specimen might not appear to be distorting, it is in fact undergoing continuous mass loss and shrinkage. Comparison of projections 1 and 150 will show marked differences attributed to non-uniform shrinkage alone. Apart from inadequately representing the specimen, alignment of the projections will be difficult unless the projections are modified after acquisition by applying stretching factors, and by accounting for non-linear movements of gold particles. Prior to acquisition, the beam is spread for 10–15 min to expose the region of interest and the surrounding area to a higher flux of electrons. This allows the region of interest to undergo gross changes prior to recording the tilt-series. Even so, further changes cannot be halted entirely—only the *rate* of change slows. To minimise further changes during data acquisition, the low-dose acquisition

procedures detailed above for cryogenic specimens may be used. Additionally, the plastic section may be introduced into the microscope via a cryo sample holder. After pre-irradiation, the sample holder dewar is filled with liquid nitrogen, and once the temperature has equilibrated to, say,  $-175\text{ }^{\circ}\text{C}$ , the tilt-series can be acquired with the least possible variation from start to finish [80, 81]. This approach results in further changes of only a few percent, making it more feasible to align the set of projections. Cooling a plastic-embedded specimen does not eliminate beam-induced shrinkage. Pre-irradiation of the specimen at room temperature is mandatory, and as a consequence, profound changes (anisotropic shrinkage and mass loss) take place prior to the acquisition of the first projection of the tilt series. The cooling serves only to minimise further changes during acquisition. As noted by Luther [82], the take-up of this cooled plastic-section technique has been low, and the “ultimate goal” should be to use vitreous specimens exclusively. In practise, however, this strategy is convenient, and its success rate in terms of yielding a ‘result’ from cellular specimens or tissues is very high. Use of this strategy should be considered in the light of the question being posed, and whether conclusions are likely to be the result of changes induced by sample processing.

The ability to record so many projections from a plastic section has resulted in a further misconception about the attainable resolution explained in terms of the Crowther criterion, which simplifies the achievable resolution by considering the number of projections and (related to this), the angular spacing of the projections. This will be discussed under the heading ‘Resolution’, suffice to say that the concept is subject to limits, and ultimately, it is meaningless in the absence of adequate sample preservation.

## 1.6 Special Acquisition Case: Block-Face SEM

The name ‘serial block-face scanning electron microscopy, SBFSEM’ was coined by Denk for a technique in which a specimen block is imaged during precise removal of sections, each of constant thickness, one layer at a time [21]. The name describes a newer focussed ion beam sectioning approach [66] equally well.

Serial block face SEM uses plastic-embedded specimens exclusively. The ability to image the face of a planed, frozen-hydrated block using cryo-SEM had been demonstrated previously [83]. This might not seem obvious, as SEM is usually thought of as a technique to visualise topography. A surface that is planed with a diamond knife is essentially flat, except for knife marks. Contrast in a cryo-SEM is typically achieved by brief etching of the surface to expose features. Etching is achieved by sublimation, which in turn is effected by raising the temperature to approximately  $-90\text{ }^{\circ}\text{C}$ , well above the devitrification temperature. Thus, devitrification has occurred, and this is likely to be the case in freeze-substitution as well. Furthermore, due to heat-transfer considerations, it is doubtful whether larger specimens ( $>200\text{ }\mu\text{m}$ ) can be vitrified in the first place. On the other hand, freeze-substitution and plastic-embedding provides specimen blocks that are readily

amenable to large-volume imaging. It is beyond the scope of this introductory chapter to outline the theory of scanning electron microscopy and focussed ion beam technology, suffice to say that the sample preparation closely resembles that of plastic blocks used for TEM tomography but with the further incorporation of/doping with heavy metals to aid in contrast and to obviate specimen charging [24, 25, 46]. The appearance of the resulting micrographs also resembles bright-field TEM micrographs. This familiar appearance means that interpretation and segmentation tasks are similar to TEM tomography of plastic sections [84] but the strategy is applicable to a much larger scale, such as whole cells. The approach is described in detail in Chap. 5

It is also worth noting at this point that scanning electron microscopes using an in-built ultramicrotome, the so-called ‘Denk technique’ [21], require a variable pressure or ‘environmental’ SEM (VP-SEM, ESEM, respectively). This is to cope with outgassing from each newly exposed resin surface, which has been discussed above in relation to mass loss. Ablation with a focussed ion beam requires a dedicated ‘dual-beam’ or ‘cross-beam’ FIB-SEM instrument. This is a scanning EM instrument with an ion beam column fitted at a fixed angle to the electron gun (the stage, however, can typically be tilted and possibly also rotated to provide maximum freedom for nanofabrication). Finally, the FIB-SEM with its highly flexible milling capabilities can be used to nanofabricate specimens for cryo- electron tomography [39, 40, 66, 67], provided that the vitrification cold-chain is uninterrupted, and that the specimen is protected from the formation of frost during transfer to the TEM. Electron diffraction studies by Marko and colleagues [85] show convincingly that the milling process does not compromise vitrification. Areas adjacent to FIB-milled lamellae are sputtered destructively, which highlights the importance of preserving target structures such that they are located within the remaining volume.

## 1.7 Alignment of Projections

A TEM projection micrograph from a thin specimen contains a wealth of 3D information, yet in the classical 2D depiction, features from multiple planes are superimposed, and the ability to determine relative depth and thereby distinguish between interconnected and discrete features is lost. For example, features may appear to be contiguous when they are in fact separate, unconnected entities lying in close proximity. The true nature of the sample densities and their spatial relationships become apparent when an aligned tilt series of projections is viewed as an image sequence. The current discussion refers almost exclusively to alignment of projections acquired by TEM tomography, where alignment is a mandatory step of the workflow. (N.B. The term ‘alignment’ is essentially synonymous with the term ‘registration’ used commonly in medical imaging.)

Unlike some related imaging techniques that operate in Fourier space, *e.g.* magnetic resonance imaging (MRI), individual projections from a TEM tilt series

require alignment to a common frame of reference prior to reconstruction. As a consequence, electron tomography reconstructions are not available in real-time. Misalignment of projections is due to the fact that cross-correlation-based tracking attempts to re-centre the region of interest at each tilt angle but in the case of low-dose tomography, this function depends on the tracking region behaving in exactly the same manner as the recording region. Even when microscope settings are optimised, unreliable tracking or cumulative translational shifts (*cf.* drift/ blurring) might be due to a slight unevenness in the grid, for example.

Alignment of projections has traditionally relied on the presence of fiducial markers to create a coordinate system for mutual alignment of the projections. In this method, colloidal gold particles are added to the specimen before plunge-freezing (cryo-tomography) or to one or both surfaces of sections (plastic or cryo, see below). The spatial coordinates of each electron-dense marker are selected in every projection to establish a common coordinate system. This requires at least 3 particles to be visible in all projections, and preferably at least 5 to account for rotations that result from variations in lens current (a nominal magnification of 20,000X might actually be 20,002X in one projection followed by, say, 19,997X in the next, and so on). Adsorbed gold colloids on plastic sections are typically numerous and distributed randomly. This allows for considerable manipulation of the aligned image stack prior to reconstruction, such that the reconstruction represents a globally corrected solution. For cryo- tomography, gold colloids are typically titrated into a suspension sample prior to vitrification. Therefore, cryo specimens typically have fewer markers per field of view, and the gold may bind preferentially to certain components. The lack of shrinkage and mass loss experienced by these samples, however, means that this is usually sufficient. For cellular samples grown on TEM sample grids, the markers can be deposited on the carbon film support prior to incubation with the cells. Alternatively, colloidal gold can be deposited onto vitreous specimens using an adaptation of the ingenious quantum dot method demonstrated by Masich *et al.* [86]. Briefly, gold colloids are functionalised with triphenylphosphine to render them soluble in toluene. The stabilised particles are dried in batches, and when required, the stabilised powder is resuspended in isopropane, which remains liquid at  $-150\text{ }^{\circ}\text{C}$ . The vitrified sample grid is dipped in the gold suspension, blotted with filter paper, and then transferred to a cryo sample holder for tomography [64]. Gold colloids are preferred to quantum dots for alignment because they offer constant contrast at all tilt angles. Quantum dots are perfect crystals. During tilting, their contrast is minimal when the plane of the crystal lattice coincides with the direction of the electron beam. They thus tend to ‘blink’ on and off, and often blend in with (low contrast) electron-dense sample features when the markers’ contrast is not at its maximum. It may be preferable to use mixtures of 10 nm and 20 nm gold colloids, in the event that the 10 nm particles become difficult to track in highly tilted projections.

Marker-free alignment, usually of the feature-tracking variety, is essential when fiducial markers are scarce or absent, when the markers are poorly distributed (*e.g.* all near the tilt axis) or when the sample does not behave as a rigid body [87, 88], such as a poorly attached cryosection. Of course, gold colloids can be selected as

features. These approaches are computationally more advanced but variants are now implemented in some commercial as well as freely available software packages. The reader is referred to the review by Amat *et al.* [89] for an in-depth discussion.

After alignment, reconstruction (see following section) is a comparatively simple task that can be executed via command line, provided that the alignment meets (user-defined) acceptable standards. For example, the operator might specify a given tolerance corresponding to sub-pixel alignment. If the pixel size at the detector corresponds to 1 nm, then sub-pixel alignment corresponds to sub-nanometre accuracy. This should not be confused with resolution in the final reconstruction. It simply means that if the alignment accuracy is better than 1 or 2 nm, then it will do justice to the expected resolution of, say, 4 nm in the final reconstruction. In other words, it does not degrade resolution.

By definition, the principle of SEM ‘slice and view’ tomography (Chap. 5) would indicate that individual slices do not require further alignment: the block is not tilted during acquisition, and the detector-block geometry is maintained throughout the process, such that sequential images should be in perfect registration as they are acquired. Specimen drift or other factors such as stage movement can lead to a translational ( $xy$ ) shift between one or more slices. These image shifts are easily corrected during or after acquisition, however, and the process can be automated. This is done most easily via a cross-correlation function, and it would make sense to include this in the workflow, even if the unaligned stack passes visual inspection. Typically, the first step in such a workflow would be to deal with the massive file size via an initial  $xy$  scaling (‘binning’) factor. Alignment could be done after this step. If dedicated functions are not provided by the system, suitable scripts/macros for this task are freely available for software such as ImageJ, although they may have been written for other techniques (*e.g.* Turboreg).

## 1.8 Reconstruction of an Aligned Tilt Series

As discussed in the preceding section, sequential micrographs acquired by slice and view SEM are by definition already registered, and as such, represent  $xy$  slices of the reconstructed volume. The remainder of this section applies to reconstruction of tilt series acquired by TEM tomography. For a more detailed discussion, see Chap. 5.

After achieving a satisfactory alignment (preferably according to some quantitative criterion), the practical execution of a reconstruction algorithm using modern software packages can be as simple as a one-step operation using default settings. This will generate a mathematically valid solution to the reconstruction problem, which can be output as an  $xy$  image stack and/or animation. The defaults would typically comprise a reconstruction of the entire volume corresponding to equal  $xyz$  dimensions. Since a slab geometry is typically characterised by  $z$  dimensions that are a small fraction of the  $xy$  area, reconstruction of equal  $xyz$  dimensions results in



a reconstruction with a huge amount of redundant space above and below the actual specimen. This can be cropped from the 3D volume to save disk space. More sophisticated software allows the user to specify the  $z$  dimensions to be reconstructed as well as any centre offset, which saves computation time, especially in the case of more intensive algorithms.

For many years, radioastronomers, medical X-ray (CT) tomographers and, more recently, electron tomographers have used reliable reconstruction algorithms based on the Radon Transform. The standard reconstruction algorithm for this purpose is the weighted back projection (syn. filtered back projection) algorithm [90]. This algorithm is based on the theorem proved mathematically by Radon in the early 1900s [91] and which was rediscovered by radioastronomers in the 1960s [92]. Typically, each image of a single-axis tilt series corresponds to a projection of the object onto a plane perpendicular to the tilt axis. In electron tomography, the intensities arise from electrons that pass through the specimen, essentially along a straight line or ‘ray’ perpendicular to the plane. The number and type of electrons reaching the detector depends on their interactions with the specimen and the electrostatic densities along a given path through the specimen [93]. Radon’s theorem explains that each real-space image corresponds to a 2D plane in Fourier space that intersects the origin and is perpendicular to the viewing axis. Back-projection algorithms make use of this theorem by repopulating the planes according to the angular projections acquired at the microscope. In real space, this is equivalent to an inverse projection operation, with the observed densities being distributed equally along the ray onto all volume elements that contribute to the projection (Fig. 1.1 (lower panel), 2, 9). Thus, back-projection algorithms are regarded as a first-order approximation to an underdetermined system of linear equations given by the projection images. Prior to summation, appropriate filtering (‘weighting’) is used to reduce artefacts caused by uneven sampling in Fourier Space (‘discretisation artefacts’), which effectively bias the distribution towards low frequencies [94].

Post-reconstruction image processing can be applied to reduce the size of the calculated volume or to make an arbitrary correction for X-axis tilt. Due to the speed and robust nature of the weighted backprojection algorithm, it is common practise to perform this calculation even if the intention is to proceed to more time-consuming, iterative reconstruction algorithms such as the algebraic reconstruction technique (ART) or simultaneous iterative reconstruction technique (SIRT). Both of these algorithms involve repeated back-projection steps [95]. ART compares the differences between the reprojections of the reconstructed volume and the measured data and corrects the volume accordingly [96, 97]. It then takes the respective difference images and multiplies them by appropriate weighting factors and adds them to the original back-projection model, and the projections are recalculated until such time as a certain stopping criterion is met. ART is computationally efficient and contains all frequency information but tends to be relatively unstable with respect to noise. The SIRT algorithm is similar to ART, but performs the update of the reconstruction volume only after all corrections have been calculated as opposed to one at a time [90, 98]. SIRT converges more slowly

but it is regarded as superior with respect to noise and artificial edge enhancements. Thus, SIRT reconstructions perform well with noisy data typical of cryo-EM and generally tend to look ‘smoother’ than the corresponding weighted backprojection. Ultimately, the choice may come down to user preference and perceived aesthetic qualities of the final result but both represent mathematically correct solutions to the backprojection problem. More importantly, the choice of reconstruction algorithm may influence the efficacy of subsequent denoising and segmentation routines. Electron tomography may yet benefit from alternative reconstruction algorithms that were abandoned originally due to (then) unrealistic computational requirements.

## 1.9 Resolution

We have already defined electron tomography as a technique capable of 4 nm resolution. Resolution is discussed in detail in Chap. 10, and in relation to subtomogram averaging below. Resolution in 3D space is not a trivial concept, and misleading claims of resolution are sometimes made due to a fundamental misunderstanding of the Crowther criterion, which relates resolution to sampling efficiency. Assuming that the object is sampled isotropically, *i.e.* the angular range is sampled evenly (which is usual for some forms of tomography but does not usually apply to electron tomography), the Crowther criterion simply states that the resolution is a function of the number of unique projections. This seems logical but it represents a theoretical or ‘best-case’ scenario. For plastic-embedded samples that seem to tolerate many projections without obvious radiation damage, it is tempting to record projections with an increment of 1 degree or less, which generates more than 150 projections. Inserting this number into the formula for the Crowther criterion produces an impressive number that certainly cannot withstand scrutiny. The obvious test of this claim is to be able to identify a feature in the tomogram that demonstrates such resolution. Resolution of better than 0.8 nm should be able to resolve alpha helices in proteins. The best resolution achieved using cryo- electron tomography does not exceed 4 nm, nor is it likely to exceed 2 nm in raw data. Information and resolution are related but information is more important than unproductive debates [4]. In practice, resolution is degraded by specimen thickness, interpolation artefacts that occur as a result of the reconstruction algorithm, and in the case of unstained specimens that require phase contrast via imposed underfocus, the contrast transfer function (CTF) determined by the chosen defocus value. The latter is of course addressed by the use of phase plate technology [99]. Perhaps more obviously, resolution is a function of the magnification, which implies that it cannot surpass the Nyquist Frequency. For a more thorough treatment of resolution in electron tomography, the reader is referred to the work of Steven [100] and the chapter by Penczek [101], as well as Chap. 9. Subtomogram averaging (see below) is a means of increasing resolution locally where structures are amenable to averaging.

## 1.10 Post-reconstruction Image Processing

This section introduces the strategies for mining the complexity of tomograms, which are covered in detail in subsequent chapters (Chaps. 8, 11 and 12). These optional techniques are segmentation, which is often aided by prior denoising, and subtomogram averaging. Template matching can be used to select subtomographic volumes for subtomogram averaging; this can be regarded as a special form of segmentation.

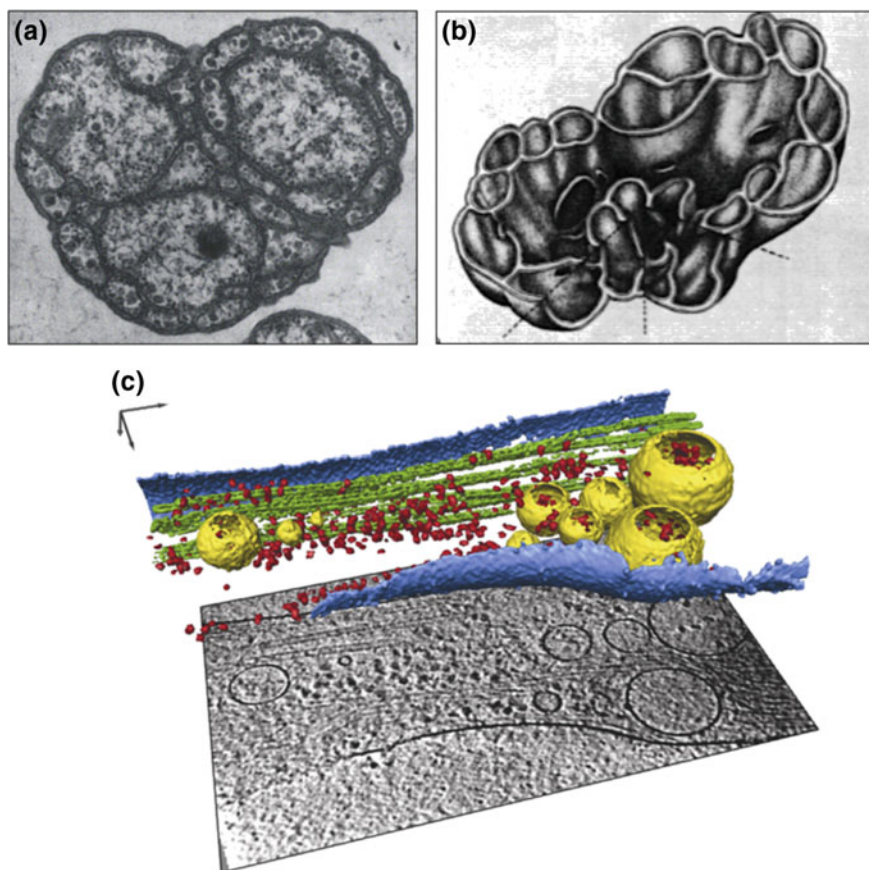


**Fig. 1.6** Progress in segmentation. Early 1970's. **a** Thin section electron micrograph of a compartmentalised bacterium and **b** 'artist's impression' of internal structure based on the micrograph and a clay model [104]; **c** surface-rendering of an appendage from a mammalian cell grown in tissue culture

### 1.10.1 Segmentation and denoising

Segmentation can be defined as the process by which electron-dense features in a tomogram are ascribed identities and highlighted relative to other features (Fig. 1.6; Chap. 12; [18]). This decomposition into structural components, *e.g.* membranes or filaments is essential to understanding function [35]. Early examples of segmentation were actual models made with, for example, ping pong balls, corks [102], balsa wood [103], and even clay [104]. Given that segmentation still tends to be time-consuming, even for a specialist, the reasons for doing so are to give clarity to the features of interest (via the use of colour and shading but also by purposefully omitting distracting features), and to present the data in a way that does justice to 3D spatial representation. Here, the benefits of tomography are finally realised. Judicious use of colour, lighting and perspective provides an intuitive representation of features in real space. There is no convention for colour-coding of features, and colours can be chosen to emphasise distinct structures and even their functional relationships. Segmentation of a 2D micrograph is certainly possible but it makes assumptions about whether features are interconnected or merely in close proximity. 2D snapshots from any plane of the reconstruction can reveal details that were not apparent from the original 2D perspective.

Computerised segmentation can be an entirely objective approach [105, 106], not to mention the least tedious. Semiautomated (semi-objective) approaches can also be highly efficient [84]. Nonetheless, tomograms are often segmented manually because the available segmentation algorithms are often inferior to human anticipation, which can infer incomplete and/or anisotropic data. Examples of features that can be delineated without *a priori* information (such as an electron-dense label) include membranes, components of the cytoskeleton, and distinctive molecular complexes such as the 26S proteasome [38]. In this case, structural signature alone is sufficient for reliable identification [107].

Stained plastic sections are dominated by amplitude contrast and a correspondingly high signal-to-noise ratio. In the simplest case, manual thresholding of intensities and removal of spurious (outlying) features may yield an acceptable result for less complex tomograms. The ‘Watershed’ algorithm and other useful segmentation methods are discussed in Chap. 12. Projections of unstained cryo specimens are dominated by (weaker) phase contrast and noise. Bilateral filtering and nonlinear anisotropic diffusion (NAD) [108] are examples of real-space, nonlinear denoising algorithms that are relatively stable with respect to noise; however, they remove some signal component selectively, resulting in data with higher SNR but suboptimal preservation of information (see Chap. 8). Therefore, denoising is suitable as an aid to segmentation but not for further quantitative analysis or subtomogram averaging.

### 1.10.2 Template matching

A special subset of segmentation is ‘motif search’ or ‘template matching’, a form of pattern recognition. This is the basis for ‘visual proteomics’ [53]. Like subtomogram averaging, it can only be performed on cryo datasets because these faithfully represent the native structure. Briefly, a tomogram of a cell contains densities corresponding to the expressed portion of the genome, the proteome. If a template structure generated by an independent technique is modified to suit the characteristics of the tomogram (CTF, resolution), then the tomogram can be searched exhaustively using this structure as a template, and cross-correlation peaks indicate the spatial coordinates of the ‘hits’ as well as the statistical likelihood of it being true (Fig. 1.7). Of course, templates can be obtained from the tomogram too. A complete set of templates allows the tomogram to be repopulated with the structures positioned at their respective 3D coordinates and correct spatial orientations.

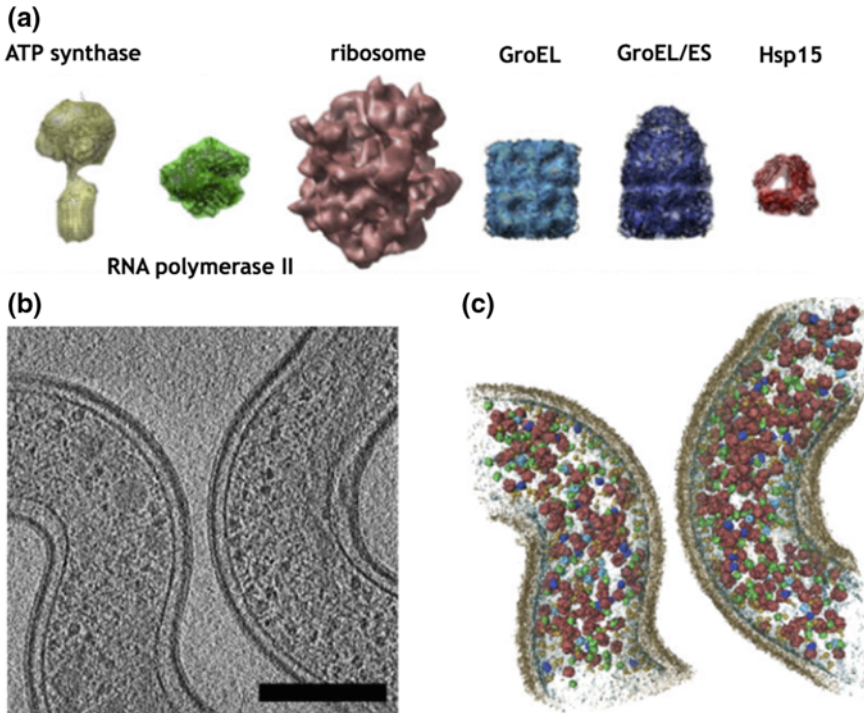


**Fig. 1.7** Visual proteomics [1, 3, 51, 52] is an approach that takes ‘high-resolution’ structures generated by single-particle analysis, X-ray crystallography and/or NMR spectroscopy, and docks these densities into the 3D space of a cell via ‘template matching’, a form of pattern recognition. The approach uses the available catalogue of possible structures, taking into account the available resolution in the tomogram. Reproduced from [51] with permission from Nature Publishing Group. Scale bar = 200 nm

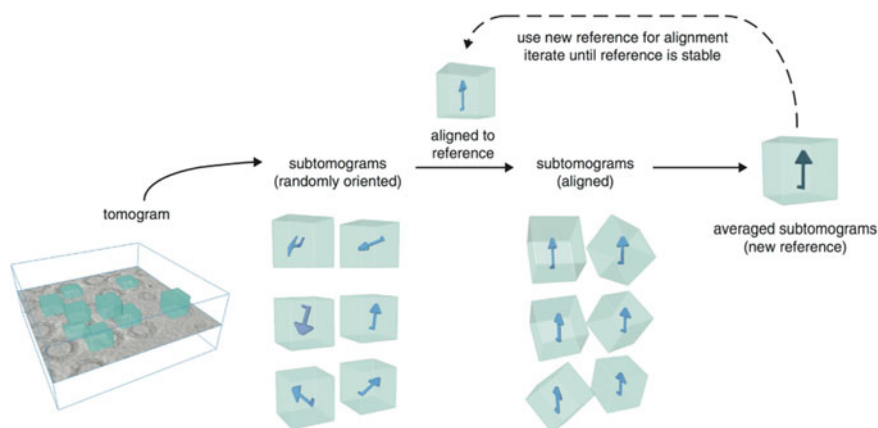


**Fig. 1.8** Strategy for subtomogram averaging (reproduced from [54], with permission from Elsevier)

### 1.10.3 Subtomogram averaging

Resolution of 4 nm must be improved upon to realise the full potential of molecular cartography, and to decipher molecular function. The best resolution that can be expected in electron tomography raw data, *i.e.* without interpolation artefacts and signal loss at the detector, might never surpass 2 nm [109]; however, this would suffice for the unambiguous structural determination of many intermediate-sized molecular complexes. The improvements required for this are now being realised via the use of phase plates [110] and direct electron detectors that account for all electrons incident on the detector [111]. Considerable information is present beyond  $(2 \text{ nm})^{-1}$ , buried in noise [52]. This information can only be extracted using filtering techniques in conjunction with *a priori* knowledge of expected structure. Another possibility is provided by subtomogram averaging. A requirement of subtomogram averaging is that the features be recognisable in the tomograms. After localising the repetitive features manually or via template matching, they are extracted *in silico*, after which the subtomograms are subjected to classification, alignment and averaging [54, 112] (Fig. 1.8). The original features in the tomograms can be replaced with the relevant averages to generate ‘synthetic’ tomograms with a superior local SNR ratio (Chap. 9). For reasons discussed previously, this is only possible using cryo- electron tomography. For example, a resolution of 7.7 Å was achieved by applying this technique to the Gag polypeptide, the major structural component of retroviruses including HIV [113]. Importantly, the technique has been quite successful for membrane-associated complexes where other structural biology techniques struggle. The reader is referred to Chap. 9 and references, *e.g.* [54], for further information.



## 1.11 Recommendations and Future Perspectives

Electron microscopes and tomography software have become very user-friendly, and they often incorporate automated column alignments that assist the acquisition process to run to completion. Alignment is now comparatively easy thanks to optimised SNR collection, smoother tracking, and flexible tilt series alignment software that automates identification and tracking of fiducial markers or other features in 3D space, perhaps by combining both strategies (treating adsorbed gold beads as ‘features’). These procedures are non-invasive—gold particles do not need to be injected destructively into the specimen prior to fixation via a gene gun - type approach.

Nevertheless, it is just as useful to identify current bottlenecks and impediments to progress. Most tomography reviews over the past 10–15 years have highlighted the need for optimised detectors, phase plates, and artefact-free specimen thinning. Efforts in these areas have led to significant improvements. The ability to make use of every (elastically scattered) electron incident on the detector surface means that information yield can be truly optimised. Of course, nothing can be done about the inelastically scattered electrons, apart from removing their collective contribution to blurring via an zero-loss energy filter [76]. Depending on the question, STEM tomography (Chap. 2) provides further flexibility for thicker specimens. The use of phase plates allows projections to be recorded close to focus, circumventing the need for CTF correction. Several studies demonstrate the success of this technology [110, 114–117]. Previously, a defined level of underfocus was required to provide optimal contrast for features of interest with a given size but at the expense of high-frequency information [118]. Volta phase plates do not suffer from fringing artefacts inherent in Zernike-type plates. They are also highly practical, allowing routine use [99, 119].

These breakthroughs in combination with true advances in sample preparation mean that single-particle cryo-EM and electron tomography have entered a new era. Vitrification is now common to both plastic and cryo workflows. Therefore, apart from the necessity to render infectious agents inactive, the artefacts of chemical fixation should no longer play a role. It is tempting to conclude that the major challenges (images acquired in focus, suitable specimen thinning procedures, close to 100% information yield from calibrated electron dose) have been addressed satisfactorily, and although there is always room for improvement, perhaps the most important point to note is that these solutions are costly in terms of instrumentation and highly-trained, dedicated personnel.

Finally, the success of standard sample collection geometries for numerous high-impact publications belies the fact that cylindrical samples have numerous advantages, including constant focus and thickness during tilting. For the last part of this chapter, I will explain why this is problematic and how this setup could help electron tomography data collection to be even more efficient, and to realise its true potential in terms of information yield.



## 1.12 The Importance of Sample Geometry

The ‘slab’ geometry common to microtome sections and vitreous thin films is suboptimal for a number of reasons. The missing (unsampled) wedge in Fourier space corresponds to information content that is substantially incomplete, and the sampled 2D planes are not sampled evenly due to the increase in apparent thickness at progressively higher tilt angles: every projection of the tilted sample is inferior to the sole projection of the untilted sample where the sample is thinnest. At progressively higher tilt, and using the same electron dose or greater for the ‘thicker’ beam cross-sections, the specimen suffers from a concomitant increase in radiation damage and degradation in resolution. In terms of all-important information yield, the reliance on a slab geometry is simply inefficient. Attempts to deal with imperfect data (reviewed in [120]) take up considerable resources [121] and makes interpretation of tomograms difficult [122]. The dual-axis acquisition scheme deals with anisotropy but only partly addresses the completeness of information. The ideal sample geometry is in fact a cylinder used in conjunction with an on-axis, rotating sample holder. With this setup, the following benefits would become apparent:

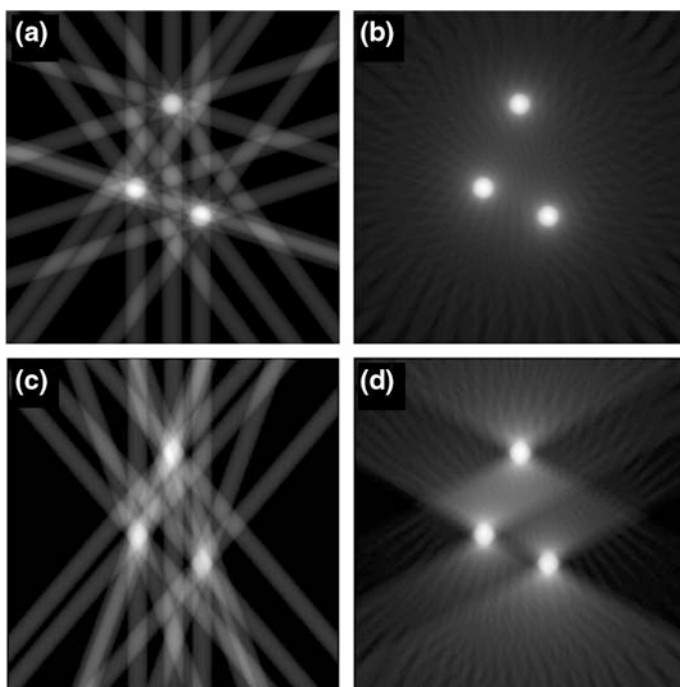


**Fig. 1.9** Effect of the missing wedge on mock 2D data. The upper panels **a**, **b** represent sampling of the full angular range ( $180^\circ$ ) achieved with an on-axis rotation holder, while the lower panels **c**, **d** represent a missing wedge of  $\pm 30^\circ$ , corresponding to a tilt range of  $120^\circ$  common to a slab geometry. **a**, **c** 5 projections; **b**, **d** 25 projections

- (1) the full angular range would be sampled. There would be no missing wedge or missing pyramid, leading to (a) simplified interpretation and (b) easier segmentation due to the fact that information is substantially complete and isotropic (Fig. 1.9);
- (2) unlike the case for slabs, there would be a negligible focus gradient across the specimen during ‘rotation’. An imposed defocus of, say,  $-5\text{ }\mu\text{m}$  would be valid for all areas, which would simplify CTF correction and would also allow the use of large-format detectors. Where phase plates are used to provide in-focus contrast, this benefit would be realised fully;
- (3) the thickness would remain constant during rotation, meaning that every projection would have identical SNR characteristics. Each projection would contribute equally to the reconstructed volume. As a corollary, radiation damage would be uniform, simplifying the dose fractionation task. For example, some acquisition schemes for plastic sections attempt to compensate for the increased beam cross-section at higher tilt by calculating the exposure time necessary to keep the brightness constant for all projections, and increase the exposure time accordingly. This leads to highly irregular distortions;
- (4) constant thickness means that fiducial markers would be equally apparent in every projection. An inability to track markers precisely or at all sometimes leads to projections of highly-tilted specimens being discarded;
- (5) larger volumes could be reconstructed: if desired, the cylindrical specimen could be slightly thicker than an untilted slab because all projections will have the same quality. Proportionally more dose could be expended on each projection. Therefore, for the same nominal resolution, the cylinder allows for a larger reconstructed volume.

In principle, cylinders of vitreous material can be manufactured by lathe using a modified cryo- ultramicrotome setup, or by focussed ion beam. Rotation sample holders for room-temperature tomography have been available for some time but an equivalent cryo- sample holder has not. The use of a vitreous cylinder was proposed in 2009 [4] and adapted for proof of principle studies of ribosomes, vesicles and bacteria [123]. Specimens that were plunge-frozen in carbon nanotubes were imaged with moderate success using a standard (tilting) goniometer, which allowed tilting to  $\pm 79^\circ$  but as noted above, with equivalent SNR in all projections. In the absence of a dedicated cryo- rotation holder, the main limit to quality seemed to be the thickness of between 400 and 800 nm, and not the carbon nanotube wall thickness of 10–20 nm, which corresponded to the thickness of amorphous carbon films used for plunge freezing. Nanotubes with an internal diameter of  $<1\text{ }\mu\text{m}$  impose restrictions on the size of specimen that can be introduced, which must be in the form of a suspension.

Although progress has been made towards nanofabrication of suitable sample geometries, targeted milling (preserving the target whilst sputtering less relevant features above and/or below the target) has only been addressed in part. Methods for localising features prior to electron tomography have been demonstrated [15, 124, 125]. These methods establish the  $xy$  coordinates of features of interest but they seldom take into account the fact that thinning (as in the case of FIB) can

inadvertently eliminate the feature of interest due to an inability to determine the position of the feature relative to the  $z$  axis.

### 1.13 Conclusion

The functions of viruses and cells are linked inextricably with structure. Electron tomography is therefore pivotal to an enhanced understanding of biology. This chapter hopefully makes clear that the practise of electron tomography has matured to the point of being useful to specialist biologists who have minimal training in physics and computer programming. A capable microscopist, however, will be able to troubleshoot effectively and adjust suboptimal beam conditions that would otherwise lead to the collection of inferior data. They will also be more wary of the numerous traps of image analysis [126].

Visualisation using electron tomography must always be considered in the light of structural preservation. Tomograms of plastic-embedded, stained samples provide information about the architecture and arrangements of organelles: ultrastructure. These amplitude contrast -dominated (stained) specimens are easier to segment, and all other factors considered, they supplant the need for stereological techniques and their assumptions. Importantly, quantitation of *e.g.* the volume fraction of mitochondria must take into account anisotropic (and frequently disregarded) shrinkage and mass loss that occurs during pre-irradiation and tilt-series acquisition. These considerations do not attempt to take into account the shrinkage, swelling, extraction, or redistribution of components that *precedes* image acquisition.

Tomograms of frozen-hydrated cells are effectively low-resolution snapshots of a cell's proteome. They are mandatory for studies of structural biology. Studies of function depend on the maintenance of spatial relationships between macromolecular assemblies. This is afforded by vitrification, which is routine for viruses and small cells [127, 128], and has become feasible for mammalian cells thanks to cryo- electron tomography of vitreous sections furnished by focussed ion beam milling [67, 129]. The majority of organelles are easily recognisable, and we have now entered an era of being able to make this claim for many large molecular assemblies *in situ*, where unambiguous structural signatures allow tomograms to be searched via sophisticated 3D cross-correlation functions. In the absence of improved resolution, smaller and/or less distinctive structures require correlative techniques for meaningful localisation. Thankfully, fluorescent and/or electron-dense markers for this purpose have been identified that are compatible with vitrification and even freeze-substitution strategies [17]. Also, photobleaching is less problematic at vitreous temperatures [130, 131].

The importance of recent developments in phase plate technology and nanofabrication cannot be understated. The next major technical advances in electron tomography are likely to emerge as a result of improvements to sample fabrication that will in turn facilitate faster and more objective 3D segmentation. Applications will benefit most from cryo-correlative microscopy, particularly sub-diffraction-limit

cryo- fluorescence microscopy [132–136], and time-resolved electron tomography of cellular events [137].

## 1.14 Protocol

This protocol is universal in the sense that low-dose acquisition schemes should be used for plastic sections as well as for beam-sensitive cryo samples. The reader should consult several such protocols, including those published by the Boulder, CO, group and the cryo protocol of Sun and Li [138].

- (1) Prepare sample according to data acquisition strategy (plastic or cryo). For detailed instructions on plunge freezing, refer to one of the numerous protocols, *e.g.*: [139–141]. Carbon-coating of plastic sections is recommended [82].
- (2) Perform all microscope column alignments, and in particular, beam tilt pivot points, tomo rotation centre, beam tilt calibrations, image (beam) calibrations, image shift pivot points, and image shift for the working magnification range.
- (3) Record a gain reference and check that it is valid via integration and/or auto-correlation (*e.g.* Digital Micrograph, Gatan, Pleasanton, CA). Determine the electron dose.
- (4) Load the sample. Plastic sections can be mounted in a cryo sample holder where available. In this case, the holder is inserted, filled with liquid nitrogen, and allowed to reach a stable temperature before continuing.
- (5) Locate the region of interest. This might be done manually or via input of coordinates obtained via fluorescence microscopy on a Finder-style sample grid, for example. Use the lowest practical magnification and enhance phase contrast by underfocussing.
- (6) Adjust the eucentric height, and focus on the specimen.
- (7) Centre the condenser aperture and adjust the gain conditions.
- (8) Align the rotation centre, preferably using gold markers.
- (9) Correct for objective astigmatism, and focus on the specimen.
- (10) Determine the possible tilt range, *i.e.* until a grid bar obscures the detector or image quality is too degraded.
- (11) Set the acquisition states for a minimum of tracking, focus and recording positions. Set the focus and tracking positions adjacent to the recording position but further along the tilt axis where the illuminated areas do not overlap.
- (12) Set the defocus value to correspond to the resolution of the target structure (not applicable for phase plate -equipped instruments).
- (13) If necessary, burn a hole in the tracking and/or focus areas by condensing the beam for a few seconds. For stained plastic sections, specify focus close to zero (say,  $-200$  nm) to ensure that the autofocus function attempts to calculate a target focus value. For plastic sections, focussing and tracking can be done on the target (recording) area but this is not recommended.

- (14) Specify the tilt series parameters including file name, tilt range, tilt increment. Also, take care to specify the image file format, and whether you wish to save individual projections or an image stack (this is not critical, as it is easy to convert between the two later).
- (15) Record the tilt series and align and reconstruct using *e.g.* IMOD [142]. Usually, a tilt log of metadata will be saved along with the image stack, specifying all acquisition conditions including tilt angles.
- (16) Save aligned image stack (optional) and reconstructed volume.
- (17) Optional steps: denoising\*, segmentation, template matching\*, subtomogram averaging\*
  - \* applicable to cryo data only

## References

1. S. Nickell et al., A visual approach to proteomics. *Nat. Rev. Mol. Cell. Biol.* **7**(3), 225–230 (2006)
2. A. Hoenger, High-resolution cryo-electron microscopy on macromolecular complexes and cell organelles. *Protoplasma* **251**(2), 417–427 (2014)
3. Asano, S., B.D. Engel, and W. Baumeister, In Situ Cryo-Electron Tomography: A Post-Reductionist Approach to Structural Biology. *J. Mol. Biol.* (2016). **428**(2 Pt A): p. 332–43
4. A. Leis et al., Visualizing cells at the nanoscale. *Trends Biochem. Sci.* **34**(2), 60–70 (2009)
5. U.E. Maurer, B. Sodeik, K. Grunewald, Native 3D intermediates of membrane fusion in herpes simplex virus 1 entry. *Proc. Natl. Acad. Sci. U. S. A.* **105**(30), 10559–64 (2008)
6. K. Iwasaki, T. Omura, Electron tomography of the supramolecular structure of virus-infected cells. *Curr. Opin. Struct. Biol.* **20**(5), 632–9 (2010)
7. I. Ibricic et al., Cryo electron tomography of herpes simplex virus during axonal transport and secondary envelopment in primary neurons. *PLoS Pathog.* **7**(12), e1002406 (2011)
8. C. Risco et al., Three-Dimensional Imaging of Viral Infections. *Annu. Rev. Virol.* **1**(1), 453–73 (2014)
9. S. Padilla-Parra, M. Tramier, FRET microscopy in the living cell: different approaches, strengths and weaknesses. *BioEssays*. **34**(5), 369–76 (2012)
10. K. Grunewald et al., Prospects of electron cryotomography to visualize macromolecular complexes inside cellular compartments: implications of crowding. *Biophys. Chem.* **100**(1–3), 577–91 (2003)
11. G. Foffi et al., Macromolecular crowding: chemistry and physics meet biology (Ascona, Switzerland, 10–14 June 2012). *Phys. Biol.* **10**(4), 040301 (2013)
12. V. Lucic, A. Leis, W. Baumeister, Cryo-electron tomography of cells: connecting structure and function. *Histochem. Cell. Biol.* **130**(2), 185–96 (2008)
13. A.V. Agronskaia et al., Integrated fluorescence and transmission electron microscopy. *J. Struct. Biol.* **164**(2), 183–189 (2008)
14. K. Cortese, A. Diaspro, C. Tacchetti, Advanced correlative light/electron microscopy: current methods and new developments using Tokuyasu cryosections. *J. Histochem. Cytochem.* **57**(12), 1103–12 (2009)
15. W. Kukulski et al., Correlated fluorescence and 3D electron microscopy with high sensitivity and spatial precision. *J. Cell. Biol.* **192**(1), 111–9 (2011)
16. R.I. Koning et al., Correlative cryo-fluorescence light microscopy and cryo-electron tomography of *Streptomyces*. *Methods Cell. Biol.* **124**, 217–39 (2014)

17. C. Loussert Fonta, B.M. Humbel, Correlative microscopy. *Arch. Biochem. Biophys.* **581**, 98–110 (2015)
18. Frank, J., ed. *Electron tomography: methods for visualization of structures in the Cell*. 2nd ed. (Springer: New York, 2006) p. 464
19. A.E. Yakushevskaya et al., STEM tomography in cell biology. *J. Struct. Biol.* **159**(3), 381–91 (2007)
20. S.G. Wolf, L. Houben, M. Elbaum, Cryo-scanning transmission electron tomography of vitrified cells. *Nat. Methods* **11**(4), 423–8 (2014)
21. W. Denk, H. Horstmann, Serial block-face scanning electron microscopy to reconstruct three-dimensional tissue nanostructure. *PLoS Biol.* **2**(11), e329 (2004)
22. M. Ballerini et al., Life science applications of focused ion beams (FIB). *Eur. J. Histochem.* **41**(Suppl 2), 89–90 (1997)
23. J.A. Heymann et al., Site-specific 3D imaging of cells and tissues with a dual beam microscope. *J. Struct. Biol.* **155**(1), 63–73 (2006)
24. G. Knott et al., Serial section scanning electron microscopy of adult brain tissue using focused ion beam milling. *J. Neurosci.* **28**(12), 2959–64 (2008)
25. G. Knott, S. Rosset, M. Cantoni, Focussed ion beam milling and scanning electron microscopy of brain tissue. *J. Vis. Exp.* **53**, e2588 (2011)
26. C. Kizilyaprak, J. Daraspe, B.M. Humbel, Focused ion beam scanning electron microscopy in biology. *J. Microsc.* **254**(3), 109–14 (2014)
27. W. Chiu et al., Electron cryomicroscopy of biological machines at subnanometer resolution. *Structure* **13**(3), 363–72 (2005)
28. J. Frank, Single-particle reconstruction of biological macromolecules in electron microscopy—30 years. *Q. Rev. Biophys.* **42**(3), 139–58 (2009)
29. C.F. Hryc, D.H. Chen, W. Chiu, Near-atomic-resolution cryo-EM for molecular virology. *Curr. Opin. Virol.* **1**(2), 110–7 (2011)
30. J. Chang et al., Reconstructing virus structures from nanometer to near-atomic resolutions with cryo-electron microscopy and tomography. *Adv. Exp. Med. Biol.* **726**, 49–90 (2012)
31. X.C. Bai, G. McMullan, S.H. Scheres, How cryo-EM is revolutionizing structural biology. *Trends Biochem. Sci.* **40**(1), 49–57 (2015)
32. E. Binshtein, M.D. Ohi, Cryo-electron microscopy and the amazing race to atomic resolution. *Biochemistry* **54**(20), 3133–41 (2015)
33. D. Elmlund, H. Elmlund, Cryogenic electron microscopy and single-particle analysis. *Annu. Rev. Biochem.* **84**, 499–517 (2015)
34. A.C. Steven, W. Baumeister, The future is hybrid. *J. Struct. Biol.* **163**(3), 186–195 (2008)
35. Plitzko, J.M. W. Baumeister, in *Cryoelectron Tomography (CET)*, in *Science of Microscopy*, ed. by P.W. Hawkes, J.C.H. Spence (Springer: New York, 2007)
36. M.G. Rossmann, Structure of viruses: a short history. *Q. Rev. Biophys.* **46**(2), 133–80 (2013)
37. C.M. Oikonomou, G.J. Jensen, A new view into prokaryotic cell biology from electron cryotomography. *Nat. Rev. Microbiol.* **14**(4), 205–20 (2016)
38. S. Asano et al., Proteasomes. A molecular census of 26S proteasomes in intact neurons. *Science* **347**(6220), 439–42 (2015)
39. B.D. Engel et al., In situ structural analysis of Golgi intracisternal protein arrays. *Proc. Natl. Acad. Sci. U. S. A.* **112**(36), 11264–9 (2015)
40. Engel, B.D., et al., Native architecture of the Chlamydomonas chloroplast revealed by in situ cryo-electron tomography. *Elife* **4** (2015)
41. J. Mahamid et al., Visualizing the molecular sociology at the HeLa cell nuclear periphery. *Science* **351**(6276), 969–72 (2016)
42. W. Hoppe et al., Three-dimensional reconstruction of individual negatively stained yeast fatty-acid synthetase molecules from tilt series in the electron microscope. *Hoppe Seylers Z. Physiol. Chem.* **355**(11), 1483–7 (1974)
43. B.J. Marsh, M. Pavelka, Viewing Golgi structure and function from a different perspective—insights from electron tomography. *Methods Cell. Biol.* **118**, 259–79 (2013)

44. C. Suarez et al., Open membranes are the precursors for assembly of large DNA viruses. *Cell. Microbiol.* **15**(11), 1883–95 (2013)
45. C. Suarez et al., African swine fever virus assembles a single membrane derived from rupture of the endoplasmic reticulum. *Cell. Microbiol.* **17**(11), 1683–98 (2015)
46. R.L. Felts et al., 3D visualization of HIV transfer at the virological synapse between dendritic cells and T cells. *Proc. Natl. Acad. Sci. U. S. A.* **107**(30), 13336–41 (2010)
47. A.A. Linaroudis, Interpretation of electron tomograms of biological specimens by means of the Scaling Index Method, in Faculty of Chemistry. Technische Universität München (2006)
48. Y. Cheng et al., A primer to single-particle cryo-electron microscopy. *Cell* **161**(3), 438–49 (2015)
49. A. Leschziner, The orthogonal tilt reconstruction method. *Methods Enzymol.* **482**, 237–62 (2010)
50. J.O. Ortiz et al., Mapping 70S ribosomes in intact cells by cryoelectron tomography and pattern recognition. *J. Struct. Biol.* **156**(2), 334–41 (2006)
51. M. Beck et al., Visual proteomics of the human pathogen *Leptospira interrogans*. *Nat. Methods* **6**(11), 817–U55 (2009)
52. F. Forster, B.G. Han, M. Beck, Visual proteomics. *Methods Enzymol.* **483**, 215–43 (2010)
53. M. Beck et al., Exploring the spatial and temporal organization of a cell's proteome. *J. Struct. Biol.* **173**(3), 483–96 (2011)
54. J.A. Briggs, Structural biology in situ—the potential of subtomogram averaging. *Curr. Opin. Struct. Biol.* **23**(2), 261–7 (2013)
55. K. Grunewald et al., Three-dimensional structure of herpes simplex virus from cryo-electron tomography. *Science* **302**(5649), 1396–8 (2003)
56. N. Grigorieff, S.C. Harrison, Near-atomic resolution reconstructions of icosahedral viruses from electron cryo-microscopy. *Curr. Opin. Struct. Biol.* **21**(2), 265–73 (2011)
57. Baker, T.S., N.H. Olson, S.D. Fuller, Adding the third dimension to virus life cycles: three-dimensional reconstruction of icosahedral viruses from cryo-electron micrographs. *Microbiol. Mol. Biol. Rev.* **63**(4), 862–922 (1999) table of contents
58. B.A. Afzelius, A.B. Maunsbach, Biological ultrastructure research; the first 50 years. *Tissue Cell* **36**(2), 83–94 (2004)
59. K.L. McDonald, R.I. Webb, Freeze substitution in 3 hours or less. *J. Microsc.* **243**(3), 227–233 (2011)
60. J.J. Woloszewick, K.R. Porter, Microtrabecular lattice of the cytoplasmic ground substance. Artifact or reality. *J. Cell. Biol.* **82**(1), 114–39 (1979)
61. J. Heuser, Whatever happened to the ‘microtrabecular concept’? *Biol. Cell* **94**(9), 561–96 (2002)
62. M.H. Ellisman, K.R. Porter, Microtrabecular structure of the axoplasmic matrix: visualization of cross-linking structures and their distribution. *J. Cell. Biol.* **87**(2 Pt 1), 464–79 (1980)
63. H. Kondo, On the real structure of the cytoplasmic matrix: learning from the embedment-free electron microscopy. *Arch. Histol. Cytol.* **58**(4), 397–415 (1995)
64. M. Gruska et al., Electron tomography of vitreous sections from cultured mammalian cells. *J. Struct. Biol.* **161**(3), 384–392 (2008)
65. T. Wagenknecht, C. Hsieh, M. Marko, Skeletal muscle triad junction ultrastructure by focused-ion-beam milling of muscle and cryo-electron tomography. *Eur. J. Transl. Myol.* **25**(1), 4823 (2015)
66. Y. Fukuda, A. Leis, A. Rigort, Preparation of vitrified cells for TEM by Cryo-FIB Microscopy, in *Biological Field Emission Scanning Electron Microscopy*, ed. by B. Humbel, R. Fleck (2016)
67. M. Marko et al., Focused-ion-beam thinning of frozen-hydrated biological specimens for cryo-electron microscopy. *Nat. Methods* **4**(3), 215–217 (2007)
68. A. Schertel et al., Cryo FIB-SEM: volume imaging of cellular ultrastructure in native frozen specimens. *J. Struct. Biol.* **184**(2), 355–360 (2013)
69. B.D. Engel, et al., Native architecture of the *Chlamydomonas* chloroplast revealed by in situ cryo-electron tomography. *Elife* **4** (2015)



70. C. Hoffmann et al., Disclosure of the mycobacterial outer membrane: Cryo-electron tomography and vitreous sections reveal the lipid bilayer structure. *Proc. Natl. Acad. Sci. U. S.A.* **105**(10), 3963–3967 (2008)
71. B. Zuber et al., Direct visualization of the outer membrane of mycobacteria and corynebacteria in their native state. *J. Bacteriol.* **190**(16), 5672–5680 (2008)
72. P.K. Luther, Sample shrinkage and radiation damage of plastic sections, in *Electron Tomography: Methods for Three-Dimensional Visualization of Structures in the Cell*, ed. by J. Frank (Springer, 2006)
73. Gordon, R., G.T. Herman, S.A. Johnson, Image reconstruction from projections. *Sci. Am.* **233**(4), 56–61, 64–8 (1975)
74. R. Hegerl, W. Hoppe, Influence of electron noise on three-dimensional image reconstruction. *Zeitschrift Naturforsch. A* **314**(12), 1717–1721 (1976)
75. B.F. McEwen, K.H. Downing, R.M. Glaeser, The relevance of dose-fractionation in tomography of radiation-sensitive specimens. *Ultramicroscopy* **60**(3), 357–73 (1995)
76. R. Grimm et al., Zero-loss energy filtering under low-dose conditions using a post-column energy filter. *J. Microsc.* **183**(1), 60–68 (1996)
77. D.N. Mastronarde, Dual-axis tomography: an approach with alignment methods that preserve resolution. *J. Struct. Biol.* **120**(3), 343–52 (1997)
78. S. Nickell et al., Pyrodictium cannulae enter the periplasmic space but do not enter the cytoplasm, as revealed by cryo-electron tomography. *J. Struct. Biol.* **141**(1), 34–42 (2003)
79. V. Lucic, F. Forster, W. Baumeister, Structural studies by electron tomography: from cells to molecules. *Annu. Rev. Biochem.* **74**, 833–65 (2005)
80. M.B. Braunfeld et al., Cryo automated electron tomography: towards high-resolution reconstructions of plastic-embedded structures. *J. Microsc.* **174**(Pt 2), 75–84 (1994)
81. M.L. Harlow et al., The architecture of active zone material at the frog's neuromuscular junction. *Nature* **409**, 479–484 (2001)
82. P.K. Luther, Sample shrinkage and radiation damage of plastic sections, in *Electron Tomography: Methods for Three-Dimensional Visualization of Structures in the Cell*, ed. by J. Frank (Springer, 2006)
83. P. Walther, M. Muller, Biological ultrastructure as revealed by high resolution cryo-SEM of block faces after cryo-sectioning. *J. Microsc.* **196**(Pt 3), 279–87 (1999)
84. A. Kreshuk et al., Automated detection and segmentation of synaptic contacts in nearly isotropic serial electron microscopy images. *PLoS ONE* **6**(10), e24899 (2011)
85. M. Marko et al., Focused ion beam milling of vitreous water: prospects for an alternative to cryo-ultramicrotomy of frozen-hydrated biological samples. *Journal of Microscopy-Oxford* **222**, 42–47 (2006)
86. S. Masich et al., A procedure to deposit fiducial markers on vitreous cryo-sections for cellular tomography. *J. Struct. Biol.* **156**(3), 461–8 (2006)
87. D. Castano-Diez et al., Fiducial-less alignment of cryo-sections. *J. Struct. Biol.* **159**(3), 413–423 (2007)
88. C.O. Sorzano et al., Marker-free image registration of electron tomography tilt-series. *BMC Bioinformatics* **10**, 124 (2009)
89. F. Amat et al., Alignment of cryo-electron tomography datasets. *Methods Enzymol.* **482**, 343–67 (2010)
90. P.F.C. Gilbert, Reconstruction of a 3-dimensional structure from projections and its application to electron-microscopy. 2. Direct methods. *Proc. Roy. Soc. London B*, **182** (1066), 89–102 (1972)
91. J. Radon, Über die Bestimmung von Funktionen durch ihre Integralwerte längs gewisser Mannigfaltigkeiten. *Berichte über die Verhandlungen der Königlich Sächsischen Gesellschaft der Wissenschaften zu Leipzig. Math. Phys. Klasse.* **69**, 262–277 (1917)
92. R.N. Bracewell, A.C. Riddle, Inversion of fan-beam scans in radio astronomy. *Astrophys. J.* **150**, 427–434 (1967)
93. R. Gordon, G.T. Herman, Reconstruction of pictures from their projections. *Graph. Image Proc.* **14**(12), 759–768 (1971)

94. G. Harauz, M. van Heel, Exact filters for general three-dimensional reconstruction. *Optik* **73**, 146–156 (1986)
95. A.P. Leis et al., Cryo- electron tomography of biological specimens: the essential role of digital signal processing. *IEEE Signal Process. Mag.* **23**(3), 95–103 (2006)
96. G.T. Herman, S. Rowland, Resolution in ART. An experimental investigation of the resolving power of an algebraic picture reconstruction technique. *J. Theor. Biol.* **33**(1), 213–23 (1971)
97. G.T. Herman, A. Lent, S.W. Rowland, ART: mathematics and applications. A report on the mathematical foundations and on the applicability to real data of the algebraic reconstruction techniques. *J. Theor. Biol.* **42**(1), 1–32 (1973)
98. P. Gilbert, Iterative methods for 3-dimensional reconstruction of an object from projections. *J. Theoret. Biol.* **36**(1), 105–117 (1972)
99. R. Danev et al., Volta potential phase plate for in-focus phase contrast transmission electron microscopy. *Proc. Natl. Acad. Sci. U. S. A.* **111**(44), 15635–40 (2014)
100. G. Cardone, K. Grunewald, A.C. Steven, A resolution criterion for electron tomography based on cross-validation. *J. Struct. Biol.* **151**(2), 117–29 (2005)
101. P.A. Penczek, Resolution measures in molecular electron microscopy. *Methods Enzymol.* **482**, 73–100 (2010)
102. D. Derosier, 3D reconstruction from electron micrographs a personal account of its development. *Methods Enzymol.* **481**, 1–24 (2010)
103. A.B. Maunsbach, B.A. Afzelius, *Biomedical Electron Microscopy: Illustrated Methods and Interpretations* (San Diego: Academic Press, 1999), p. 548
104. S.W. Watson et al., A lobular, ammonia-oxidizing bacterium, *Nitrosolobus multiformis* nov.gen.nov.sp. *Arch. Mikrobiol.* **76**(3), 183–203 (1971)
105. A. Rigort et al., Automated segmentation of electron tomograms for a quantitative description of actin filament networks. *J. Struct. Biol.* **177**(1), 135–44 (2012)
106. M. Rusu et al., Automated tracing of filaments in 3D electron tomography reconstructions using Sculptor and Situs. *J. Struct. Biol.* **178**(2), 121–8 (2012)
107. O. Medalia et al., Macromolecular architecture in eukaryotic cells visualized by cryoelectron tomography. *Science* **298**(5596), 1209–13 (2002)
108. A.S. Frangakis, R. Hegerl, Noise reduction in electron tomographic reconstructions using nonlinear anisotropic diffusion. *J. Struct. Biol.* **135**(3), 239–50 (2001)
109. R. Henderson, Realizing the potential of electron cryo-microscopy. *Q. Rev. Biophys.* **37**(1), 3–13 (2004)
110. Y. Fukuda et al., Electron cryotomography of vitrified cells with a Volta phase plate. *J. Struct. Biol.* **190**(2), 143–54 (2015)
111. G. McMullan et al., Enhanced imaging in low dose electron microscopy using electron counting. *Ultramicroscopy* **109**, 1411–1416 (2009)
112. F. Forster et al., Retrovirus envelope protein complex structure in situ studied by cryo-electron tomography. *Proc. Natl. Acad. Sci. U. S. A.* **102**(13), 4729–34 (2005)
113. F.K. Schur et al., Structure of the immature HIV-1 capsid in intact virus particles at 8.8 Å resolution. *Nature* **517**(7535), 505–8 (2015)
114. K. Murata et al., Zernike phase contrast cryo-electron microscopy and tomography for structure determination at nanometer and subnanometer resolutions. *Structure* **18**(8), 903–12 (2010)
115. K. Nagayama, Biological applications of phase-contrast electron microscopy. *Methods Mol. Biol.* **1117**, 385–99 (2014)
116. G.P. Kishchenko et al., Effect of fringe-artifact correction on sub-tomogram averaging from Zernike phase-plate cryo-TEM. *J. Struct. Biol.* **191**(3), 299–305 (2015)
117. T.H. Sharp, A.J. Koster, P. Gros, Heterogeneous MAC Initiator and Pore Structures in a Lipid Bilayer by Phase-Plate Cryo-electron Tomography. *Cell. Rep.* **15**(1), 1–8 (2016)
118. J. Dubochet, et al., *CEMOVIS: Cryo-electron microscopy of vitreous sections*, in *Handbook of Cryo-Preparation Methods for Electron Microscopy*, ed. by B. Humbel D. Spehner (CRC Press: Boca Raton, 2009) pp. 259–289

119. R. Danev, W. Baumeister, Cryo-EM single particle analysis with the Volta phase plate. *Elife* **5** (2016)
120. M.F. Schmid, C.R. Booth, Methods for aligning and for averaging 3D volumes with missing data. *J. Struct. Biol.* **161**(3), 243–8 (2008)
121. L. Kovacic et al., A simple Fourier filter for suppression of the missing wedge ray artefacts in single-axis electron tomographic reconstructions. *J. Struct. Biol.* **186**(1), 141–52 (2014)
122. B. Turonova, L. Marsalek, P. Slusallek, On geometric artifacts in cryo electron tomography. *Ultramicroscopy* **163**, 48–61 (2016)
123. C.M. Palmer, J. Lowe, A cylindrical specimen holder for electron cryo-tomography. *Ultramicroscopy* **137**, 20–9 (2014)
124. W. Kukulski et al., Precise, correlated fluorescence microscopy and electron tomography of lowicryl sections using fluorescent fiducial markers. *Methods Cell. Biol.* **111**, 235–57 (2012)
125. J. Arnold et al., Site-specific cryo-focused ion beam sample preparation guided by 3d correlative microscopy. *Biophys. J.* **110**(4), 860–9 (2016)
126. R. Henderson, Avoiding the pitfalls of single particle cryo-electron microscopy: einstein from noise. *Proc. Natl. Acad. Sci. U.S.A.* **110**(45), 18037–18041 (2013)
127. G.P. Henderson, L. Gan, G.J. Jensen, 3-D ultrastructure of *O. tauri*: electron cryotomography of an entire eukaryotic cell. *PLoS ONE* **2**(8), e749 (2007)
128. M.M. Farley et al., Minicells. Back in Fashion. *J. Bacteriol.* **198**(8), 1186–95 (2016)
129. A. Rigort et al., Focused ion beam micromachining of eukaryotic cells for cryoelectron tomography. *Proc. Natl. Acad. Sci. U.S.A.* **109**(12), 4449–4454 (2012)
130. W.E. Moerner, M. Orrit, Illuminating single molecules in condensed matter. *Science* **283** (5408), 1670–6 (1999)
131. C.L. Schwartz et al., Cryo-fluorescence microscopy facilitates correlations between light and cryo-electron microscopy and reduces the rate of photobleaching. *J. Microsc.* **227**(Pt 2), 98–109 (2007)
132. E. Betzig et al., Imaging intracellular fluorescent proteins at nanometer resolution. *Science* **313**(5793), 1642–1645 (2006)
133. Y.W. Chang et al., Correlated cryogenic photoactivated localization microscopy and cryo-electron tomography. *Nat. Methods* **11**(7), 737–9 (2014)
134. R. Kaufmann, C. Hagen, K. Grunewald, Fluorescence cryo-microscopy: current challenges and prospects. *Curr. Opin. Chem. Biol.* **20**, 86–91 (2014)
135. R. Kaufmann et al., Super-resolution microscopy using standard fluorescent proteins in intact cells under cryo-conditions. *Nano. Lett.* **14**(7), 4171–5 (2014)
136. G. Wolff, et al., Towards correlative super-resolution fluorescence and electron cryo-microscopy. *Biol. Cell.* (2016)
137. W. Kukulski et al., Plasma membrane reshaping during endocytosis is revealed by time-resolved electron tomography. *Cell* **150**(3), 508–20 (2012)
138. J. Sun, H. Li, How to operate a cryo-electron microscope. *Methods Enzymol.* **481**, 231–49 (2010)
139. C.V. Iancu et al., Electron cryotomography sample preparation using the Vitrobot. *Nat. Protoc.* **1**(6), 2813–2819 (2006)
140. R.A. Grassucci, D.J. Taylor, J. Frank, Preparation of macromolecular complexes for cryo-electron microscopy. *Nat. Protoc.* **2**(12), 3239–3246 (2007)
141. G.P. Resch et al., Immersion freezing of cell monolayers for cryo-electron tomography. *Cold. Spring. Harb. Protoc.* **2011**(7), 815–23 (2011)
142. J.R. Kremer, D.N. Mastronarde, J.R. McIntosh, Computer visualization of three-dimensional image data using IMOD. *J. Struct. Biol.* **116**(1), 71–6 (1996)

Cellular Imaging

Electron Tomography and Related Techniques

Hanssen, E. (Ed.)

2018, XIX, 323 p. 84 illus., 59 illus. in color., Hardcover

ISBN: 978-3-319-68995-1